A transfer function approach for predicting rare cell capture microdevice performance

James P. Smith[1,3] · Brian J. Kirby[1,2]

Abstract Rare cells have the potential to improve our understanding of biological systems and the treatment of a variety of diseases; each of those applications requires a different balance of throughput, capture efficiency, and sample purity. Those challenges, coupled with the limited availability of patient samples and the costs of repeated design iterations, motivate the need for a robust set of engineering tools to optimize application-specific geometries. Here, we present a transfer function approach for predicting rare cell capture in microfluidic obstacle arrays. Existing computational fluid dynamics (CFD) tools are limited to simulating a subset of these arrays, owing to computational costs; a transfer function leverages the deterministic nature of cell transport in these arrays, extending limited CFD simulations into larger, more complicated geometries. We show that the transfer function approximation matches a full CFD simulation within 1.34 %, at a 74-fold reduction in computational cost. Taking advantage of these computational savings, we apply the transfer function simulations to simulate reversing array geometries that generate a "notch filter" effect, reducing the collision frequency of cells outside of a specified diameter range. We adapt the transfer function to study the effect of off-design boundary conditions (such as a clogged inlet in a microdevice) on overall performance. Finally, we have validated the transfer function's predictions for lateral displacement within the array using particle tracking and polystyrene beads in a microdevice.

Keywords Rare cell capture · Circulating tumor cell · CTC · Transfer function · Collision dynamics · Cell capture · Design optimization

1 Introduction

Rare cells have the potential to improve our understanding of biological systems, how we treat disease, and to serve as biomarkers for disease detection in the absence of other symptoms. Fetal cells circulating in maternal blood present a non-invasive alternative to amniocentesis (Mohamed et al. 2007), reducing the risk to the fetus. Stem (Zhu et al. 2013) and progenitor cells (Hatch et al. 2011) have been used for culture and later experimentation, including transplantation (Zhu et al. 2014). Circulating epithelial cells (CECs) of pancreatic origin have been found in the blood of pancreatic cyst patients, and may enable the early detection of pancreatic cancer (Thege et al. 2014; Rhim et al. 2014). Finally, circulating tumor cells (CTCs), which are shed from a primary tumor into the circulatory system and are thought to contribute to metastasis (Maheswaran and Haber 2010), can inform patient prognosis (Cristofanilli et al. 2004), therapeutic efficacy (Kirby et al. 2012; Stott et al. 2010), and the genetics of disseminating cancer cells (Russnes et al. 2010; Navin et al. 2011; Pratt et al. 2014; Lohr et al. 2014). A challenge in studying these cells is that they are exceedingly rare—as

✉ Brian J. Kirby
kirby@cornell.edu

1   Sibley School of Mechanical and Aerospace Engineering, Cornell University, Ithaca, NY 14853, USA

2   Division of Hematology and Medical Oncology, Department of Medicine, Weill Medical College of Cornell University, New York, NY 10065, USA

3   Present address: Massachusetts Institute of Technology Lincoln Laboratory, Lexington, MA 02420, USA

few as 1 CTC per 100 million blood cells, for example (Racila et al. 1998; Krivacic et al. 2004)—requiring engineered solutions to isolate as many of the target cells as possible, while capturing few blood cells.

A variety of techniques can be used to isolate rare cells (Pratt et al. 2011). Differences in size compared to non-target cells enable filtration (Hsu et al. 2008; Sollier et al. 2014), the passive focusing of cells using microvortex–wall interactions (Hsu et al. 2008; Sollier et al. 2014), and streamline-separation approaches (Gleghorn et al. 2010; Bhagat et al. 2011) or high throughput. Changes in the cell membrane composition can lead to a differential electrokinetic response (Becker et al. 1995; Shim et al. 2013; Huang C et al. 2014). Finally, surface markers unique to the target rare cell, perhaps either due to its non-hematological origin or a specific disease state, can be used to identify the cells by staining with a fluorescently-conjugated antibody and to capture cells by antibody immobilization; the latter process is known as immunocapture.

Immunocapture relies on bringing target cells into contact with an antibody-functionalized surface at conditions (e.g., local shear stress) and for a duration conducive to rare cell capture (Smith et al. 2012). Magnetic techniques mix antibody-functionalized nanoparticles (Allard et al. 2004; Hayes et al. 2006) or rods with a blood sample (Talasaz et al. 2009; Powell et al. 2012; Earhart et al. 2014), often after pre-processing steps such as centrifugation or dilution; the antibodies on the particle or rod surfaces bind with the antigens on the cell surface and then can be separated from the bulk sample by applying a magnetic field. Microdevice techniques engineer device geometries on the scale of the target cells and use combinations of diffisional mixing, cell-wall interactions, and varying shear stress to isolate rare cells by bringing them into contact with a fixed, antibody-functionalized device wall; these devices have used micron-scale obstacles in linear arrays (Nagrath et al. 2007) and radial arrays (Murlidhar et al. 2014), herringbone-like device floors to increase and control the frequency of interactions between the cells and the capture surface.

Of the techniques described, the most broadly impactful and influential techniques have been immunocapture-based, starting with the magnetic-bead-based isolation approach that evolved to become the Veridex CellSearch system (Racila et al. 1998) and later driven by the first implementation in a microfluidic platform (Nagrath et al. 2007). These approaches have led to an explosion of technological development associated with optimization of cell capture (Stott et al. 2010; Yu et al. 2014), reduction of contaminants (Gleghorn et al. 2010), expansion of downstream analyses (Stott et al. 2010; Maheswaran et al. 2008; Ligthart et al. 2013), and correlation of clinical outcomes (Cristofanilli et al. 2004; Allard et al. 2004). Our work falls into this

context, in that delineation of proper microfluidic geometries optimizes capture and minimizes contaminants.

We have previously reported on geometrically enhanced differential immunocapture (GEDI), which uses both size differences and antibody specificity to capture target rare cells, while simultaneously minimizing contaminating cell capture (Gleghorn et al. 2010; Kirby et al. 2012). GEDI uses an array of obstacles in a microfluidic device, arranged to generate size-dependent cell trajectories, bringing target cells into contact with as many obstacles as possible. Those cells are then captured on the obstacle by use of a target-specific antibody immobilized on the surface. The inadvertent capture of non-target cells is minimized by a combination of differential collision dynamics, shear stress, and antibody specificity. Figure 1 shows a potential GEDI geometry, in which cell transport and capture are governed by the array geometry (row spacing Γ, column spacing Λ, row offset Δ, obstacle diameter $2R$), cell diameter $2a$, and the mean fluid velocity U_{inlet} (which determines the shear stress and residence time a cell experiences while in contact with the obstacle surface).

Each downstream application for rare cell capture requires its own balance of capture efficiency (capturing as many target cells as possible) and sample purity (minimizing the capture of contaminating cells); e.g., genetic assays require a high purity sample of only a few cells, whereas staining and enumeration studies are more tolerant of contaminants but need many target cells for sensitivity. These challenges, coupled with the limited supply of patient samples, motivate the development of engineering tools to optimize application-specific device designs.

Existing tools to optimize the array geometry have used analytical approximations (Inglis et al. 2006; Davis et al. 2006) or computational fluid dynamics (CFD) simulations for a small subset of the obstacle array (tens of obstacles), as simulations of collision and capture dynamics in a full-size device (thousands of obstacles) is computationally challenging (Gleghorn et al. 2013; Smith et al. 2014). This work presents a *transfer function* approach that leverages those existing CFD simulations as the basis of a computationally-efficient simulation of a large device geometry, including spatially varying geometries and/or off-design boundary conditions.

In the high Péclet number regime in which most rare cell capture microdevices operate, advection dominates Brownian diffusion. Further, if we consider dilute cell suspensions (or approximate dense suspensions as dilute), a cell's trajectory through the device is a deterministic function of its size, initial position, and the array geometry. We can reduce the obstacle array to one "unit structure" around an individual obstacle, with periodic boundary conditions, and calculate transfer functions that approximates transport behavior as a function of the cell's initial position when it enters the
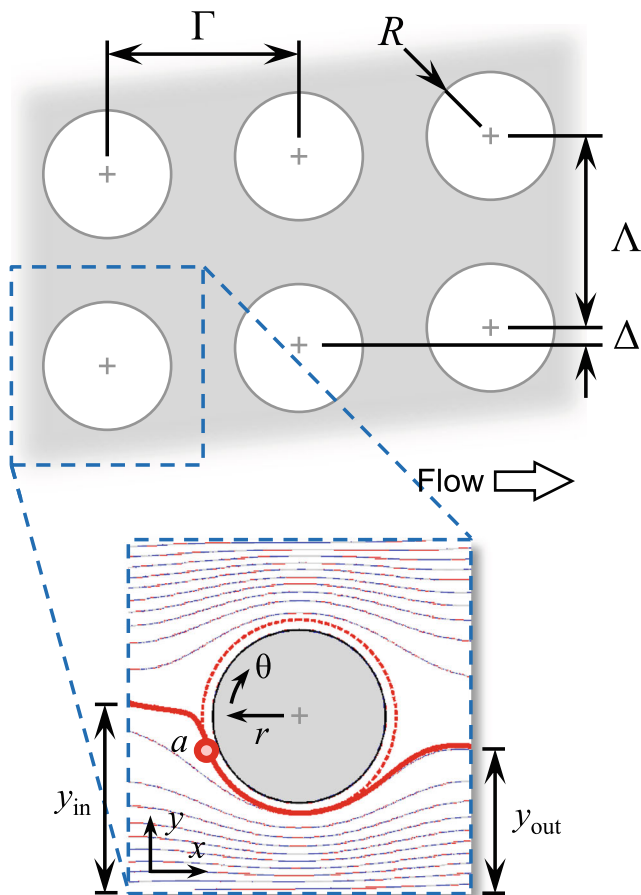
Fig. 1 A two-dimensional array of cylindrical obstacles in a microfluidic device generates size-dependent cell transport as a function of the mean velocity U_{inlet}, row spacing Γ, column spacing Λ, row offset Δ, obstacle diameter $2R$, and cell diameter $2a$. Some aspects of these arrays can be reduced to a "unit structure" with periodic boundary conditions (inset). Cell displacement ($y_{out} - y_{in}$), collision status, and shear history can be represented by a transfer function within each unit structure

function can be calculated using CFD simulations of one unit structure and applied iteratively to simulate a device of arbitrary size and spatially-varying geometry. The resulting trajectory and shear stress time histories are used in previously-validated cell capture simulations, informing the selection of a device geometry that is optimized for a specific application.
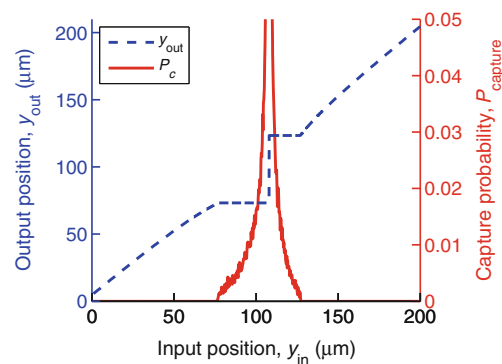
2.1 Calculating the transfer function

Particle trajectories were calculated for one unit structure using the CFD and particle advection simulation we have previously reported (Gleghorn et al. 2013; Smith et al. 2014), and used to calculate transfer function lookup tables. This process occurs in three distinct numerical simulations that are repeated for each geometry and cell diameter of interest. Briefly:

Computational fluid dynamics (CFD) simulations COMSOL Multiphysics (COMSOL, Inc.) solved the two-dimensional Navier–Stokes equations, computing the fluid velocity field for each obstacle array geometry in a small domain of 5 × 20 obstacles (chosen based on a convergence study) with an inlet velocity $U_{inlet} = 100 \ \mu m \ s$ and a zero-pressure outlet. In this system, the Reynolds number is small as compared to unity,

$$Re_\Gamma \equiv \frac{\rho U_{inlet} \Gamma}{\mu} = 0.02, \tag{1}$$

2 Computational methods

A transfer function, $H(\text{in})$, predicts output position (y_{out}), collision status ($C = 0$ or 1), and shear stress and time history ($\tau(t)$, if cell-obstacle contact occurs). The transfer

unit structure, $H(y_{in})$, subject to the limitations discussed in Section 2.2. Transfer functions can be generated for the output position, y_{out}; a collision status flag, C (0 or 1); and, if a collision does occur, the shear stress vs. time history, $\tau(t)$ experienced by that cell, which facilitates calculating the probability of cell capture (Fig. 2). The transfer function can be applied iteratively to simulate cell capture and transport in a device of arbitrary length.

Fig. 2 A transfer function can be calculated using a limited CFD and particle advection simulation of one unit structure, then applied iteratively to simulate an arbitrarily large obstacle array device. Output position (y_{out}), collision status and shear history (τ vs. t; not shown), and thus the probability of capture (P_c) for a given cell type are deterministic functions of a cell's input position (y_{in}) in the high Péclet number regime where most obstacle array microdevices operate. There is a characteristic discontinuity in y_{out} at the stagnation point on the obstacle's leading edge, which occurs at $y_{in} \approx \Gamma/2 + \Delta = 108 \ \mu m$, and correspondingly $P_{capture} = 1$ at that stagnation point; both of these characteristics are mitigated by diffusion in physical systems. Here, capture probability is shown for a 20 μm diameter LNCaP prostate cancer cell in a $\Gamma = \Lambda = 200 \ \mu m$, $\Delta = 8 \ \mu m$ device with $U_{inlet} = 100 \ \mu m \ s$

where ρ and μ are the bulk fluid density and viscosity, respectively; the flow is independent of U_{inlet}. From this data, x- and y-velocity components for the unit structure encompassing the central obstacle (which has periodic boundary conditions) were interpolated onto a regular grid and saved. This process is repeated for each array geometry.

Particle advection simulations The velocity field data calculated above is then used in a custom, parallelized particle advection simulation realized in MATLAB (The Mathworks). An initially uniform distribution of cells is advected through the unit structure by use of a fourth-order Runge–Kutta integration scheme with adaptive time stepping. In this system, advection dominates diffusion and inertial effects are negligible (Pe, the Péclet number, $\gg 1$), so the cells are modeled as Lagrangian tracers, following the fluid streamlines unless cell–obstacle contact occurs; at which point, cells roll along the obstacle surface. This process is repeated for a range of cell diameters and array geometries of interest.

Transfer function derivation The particle advection results are used to derive several transfer function lookup tables, $H(y_{\text{in}})$, that are unique to each geometry and cell diameter. The output position, y_{out}, and a cell-obstacle collision flag, C, are saved for each y_{in} value. If a collision occurs (i.e., $C = 1$), the x- and y-velocity fields are used to calculate the shear stress experienced by the cell as it rolls along the obstacle surface, $\tau(t)$. An illustrative transfer function for y_{out}, as well as the capture probability expected for LNCaP prostate cancer cells (calculated as described in Section 2.3) given the shear stress time history transfer functions, is plotted in Fig. 2.

2.2 Simulating cell transport using the transfer function

A MATLAB simulation was developed to iteratively apply the transfer function lookup tables, calculated as described in the previous section, to calculate trajectories for an initially uniform distribution of cells in a device of arbitrary size.

For each unit structure along the length of the device, each starting particle's trajectory is calculated using one-dimensional linear interpolation of the transfer function lookup table, $H(y_{\text{in}})$,

$$y_{\text{out}} = H_{\text{position}}(y_{\text{in}}), \tag{2}$$

where y_{in} and y_{out} are the particle's position with respect to that unit structure's local coordinate system. The same interpolation process is used for the collision status flag, C,

$$C = \lceil H_{\text{collision flag}}(y_{\text{in}}) \rceil, \tag{3}$$

and, if contact occurs (i.e., $C = 1$), the shear stress history,

$$\tau(t) = H_{\text{shear history}}(y_{\text{in}}). \tag{4}$$

The local values from unit structure N are advanced into unit structure $N + 1$ accounting for the shift in local coordinates due to the offset, Δ,

$$y_{\text{in},N+1} = y_{\text{out},N} - \Delta. \tag{5}$$

This process is repeated for each particle start position and each unit structure in the device, with the mean of C for all start positions and unit structures representing the mean collision frequency for that cell diameter and geometry. Shear histories, $\tau(t)$, for each particle start position are saved for subsequent use in a Monte Carlo cell capture simulation, described in Section 2.3.

We can also approximate changes in the offset (both magnitude and direction) between unit structures simply by using a different transfer function lookup table along the length of the device. This approximation assumes that the fluid velocity field—and thus the transfer function, $H(y_{\text{in}})$—within each unit structure is unaffected by offset changes between it and adjacent unit structures, and is only valid when there are few changes in offset as compared to the number of unit structures in the device.

2.3 Predicting cell capture probability

Shear histories, $\tau(t)$, generated by the transfer function for each starting particle were used to calculate cell capture probabilities using the exponential cell capture model that we have reported previously (Smith et al. 2014). Briefly:

Modeling cell capture The most sophisticated cell capture models include the effects of mechanical forcing, cell adhesion kinetics (Bell et al. 1984; Dembo et al. 1988), cell deformation, and biomolecule deformation (Dustin et al. 1996; Zhu et al. 2000). Although these detailed models are able to predict cell adhesion, cell release, and rolling (i.e., repeated adhesion and release) events, they require *a priori* knowledge of the many parameters that describe these adhesion events, such as reaction rate coefficients and contact area measurements.

Because these parameters are often unknown for rare cell capture applications, we have pursued a reduced-order model to create an engineering tool based on the limited information available for these cells. We began with a shear-stress dependent capture model first reported by Decuzzi and Ferrari (2006) and subsequently used to predict cancer cell capture in microfluidic devices by Wan et al. (2011),

$$P_{\text{capture}} = m_r m_l K_a^0 A_c \exp\left(-\frac{\lambda}{k_B T}\frac{F_{\text{dislodge}}}{m_r A_c}\right), \tag{6}$$

where the probability of cell capture (P_{capture}) is a function of the receptor and ligand surface densities (m_r and m_l, respectively), receptor–ligand association constant at zero load (K_a^0), the contact area (A_c), the characteristic receptor–ligand bond length (λ), the thermal energy ($k_B T$), and the dislodging force (F_{dislodge}). We grouped the constants, which are unknown for most rare cell systems, into two lumped parameters, took F_{dislodge} as proportional to the local shear stress τ, and discretized the model as

$$\mathrm{d}P_{\text{capture}} = A \exp\left(-B\tau\right)\,\mathrm{d}t, \tag{7}$$

where $\mathrm{d}t$ is the length of each timestep in the simulation, and $\mathrm{d}P_{\text{capture}}$ is the probability that capture occurs in that timestep. The constants A and B are experimentally-determined, unique to cell type and surface chemistry system, and are measured by data fitting (Smith et al. 2014) to the results of capture characterization experiments in a Hele-Shaw flow chamber designed to expose cells to a range of shear stresses (Santana et al. 2012; Huang et al. 2014). This work uses LNCaP human prostate adenocarcinoma cells and J591, a monoclonal antibody that binds to the prostate-specific membrane antigen (PSMA) expressed on the LNCaP cell membrane, as a model system. The capture constants for this system have been previously reported as $A = 3.44 \times 10^{-2}$ s^{-1} and $B = 85.5$ Pa^{-1} (Smith et al. 2014).

Cell capture Monte Carlo simulations The discrete cell capture probability, $\mathrm{d}P_{\text{capture}}$ (Eq. 7), was calculated for each timestep where contact occurred using the shear histories, $\tau(t)$, generated by the transfer function for each starting particle. This discrete probability was compared to a pseudorandom number, $\mathrm{d}P_{\text{random}}$; a cell was assumed "captured" if $\mathrm{d}P_{\text{capture}} \geq \mathrm{d}P_{\text{random}}$. This stochastic process was repeated as a Monte Carlo simulation, varying $\mathrm{d}P_{\text{random}}$ for 1000 replicates per particle trajectory (with the number of replicates chosen based on a convergence study), and the average value reported as the mean capture probability for that cell and array geometry.

3 Experimental methods

The displacement transfer function (y_{out} vs. y_{in}) was determined experimentally for particles flowing through the GEDI microdevice reported by Gleghorn et al. (2010) and Kirby et al. (2012). These experimental measurements were compared to the CFD-derivedtransfer functions for the same geometry and particle diameter with various boundary condition errors, with the best-fit result quantifying the error present in the physical GEDI device owing to flow perturbations due to the inlet/outlet design, as well as the effects of the three-dimensional nature of flow in the GEDI device.

3.1 Particle tracking experiments

A GEDI microdevice was prepared as described by Gleghorn et al. (2010). Briefly, a $\Gamma = \Lambda = 200\ \mu m$ array of $2R = 100\ \mu m$ obstacles with an offset of $\Delta = 7\ \mu m$ was etched into silicon at a depth of $100\ \mu m$ using standard photolithography techniques. The device was sealed using a 3-mm-thick polydimethylsiloxane (PDMS, 7:1 base:curing agent) gasket held in place with a plexiglass compression jig. Tygon tubing (0.010 inch inner diameter; Saint-Gobain) was connected to a 3 mL plastic syringe (Becton Dickinson) and the device was manually primed with deionized water.

Polystyrene beads (Bangs Laboratories; 20.92 ± 0.64 μm diameter) were suspended into a density-matched water/glycerol solution (1.026 g/mL) at a concentration of 10^6 beads per mL. Pluronic F68 non-ionic surfactant (Sigma-Aldrich) at a concentration of 0.1 % (v/v) was added to the bead suspension to reduce non-specific adhesion of the beads to themselves and to the microdevice surface.

The bead suspension was pumped through the microdevice using a 3 mL syringe and a syringe pump (Chemyx) at a rate of 1 mL/hr for the duration of the experiment. After the bead suspension had flushed out the device, a region of approximately 3×3 obstacles (centered across the device width and adjacent to the inlet) was imaged at $20\times$ in bright-field using a Nikon Eclipse LV-100 microscope, Q-Imaging EXi Blue CCD camera, and Nikon NIS-Elements imaging software. 2×2 binning resulted in the acquisition of 696×520 pixel images at approximately 18 frames/s; these frames were saved as a series of grayscale uncompressed TIFF images.

3.2 Image processing

TIFF images were processed using the MATLAB adaptation (Blair and Dufresne 2007) of the well-known IDL Particle Tracking software (Crocker and Weeks 1996). Briefly: images are first rotated to align the coordinate system of the array with that of the image, then are color-inverted to present bright beads on a dark background. Next, a spatial band-pass filter is applied to remove the background and smooth out the beads, with a spatial cutoff chosen based on the bead diameter. The centroid of each bead is then determined by identifying the local brightness maxima in each image to pixel level accuracy. Finally, sequential pairs of images are compared and $\langle x, y \rangle$ tracks for each particle identified.

Each particle trajectory is compared to the known boundaries of the unit structures present in the image. Particle tracks which are long enough to traverse across a complete unit structure are used to compute y_{out} as a function of
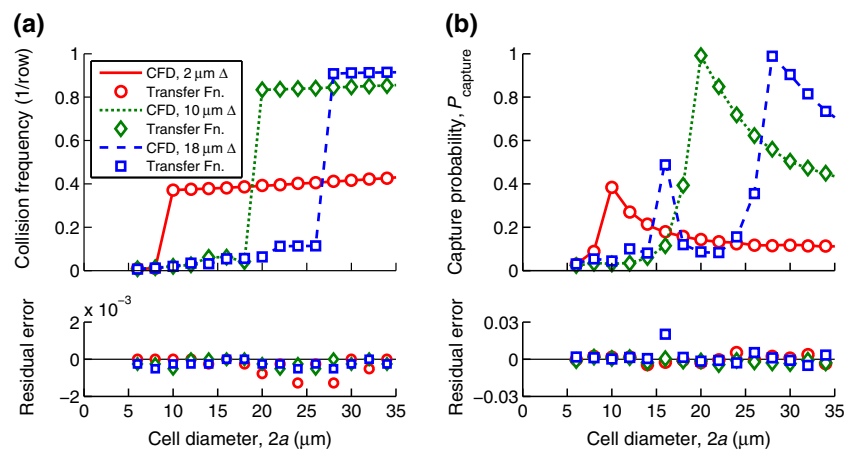
Fig. 3 The transfer function model (symbols) closely agrees with the full CFD simulation (lines) for both **(a)** collision frequency and **(b)** capture probability using LNCaP prostate cancer cells and a device with $N = 100$ unit structures for a range of offsets (Δ). The residual error (e.g., $P_{capture, CFD} - P_{capture, Trans. Fn.}$) quantifies the error between the transfer function approximation and the CFD simulation, and the residual error for collision frequency and capture probability are shown below their respective plots. The RMS residual error across all values of Δ (i.e., $\Delta = 0$ to $\Gamma/2$) and cell diameters studied is 1.01×10^{-2} row^{-1} for collision frequency and 1.34×10^{-2} for capture probability, with a 74-fold reduction in computational time

y_{in} using two-dimensional linear interpolation across each boundary. Incomplete tracks (i.e., trajectories that terminate before leaving the unit structure), which are common for particles that slow down significantly near the stagnation region at the front of the obstacle and are "lost" by the tracking code in the dark region caused by the fillet between the floor of the device and each cylindrical obstacle, are discarded. y_{out} vs. y_{in} data points from individual particles are binned into 20 y_{in} groups for statistical purposes; the mean y_{out} value for each y_{in} bin is reported in this work, along with error bars representing the standard error of the mean to a 95 % confidence interval.

The experimentally derived transfer function was compared to CFD-derived transfer functions for the same particle and array geometry with various errors in the boundary conditions (i.e., an off-design transverse flow component), calculated as described in Section 2.1. A simulated transfer function was selected that minimized the overall error residual between it and the experimental transfer function; with this transfer function corresponded to the off-design flow error in the experiment (E; see Eq. 8) within ± 1 %.

4 Results and discussion

Here, we present a validation of the transfer function model, by comparison to our previously described CFD (Gleghorn et al. 2013; Smith et al. 2014) simulations for simple geometries and experimental measurement of the position transfer function. We then apply the transfer function simulation to study complex geometries and boundary conditions beyond the capabilities of the CFD simulation, at a significantly reduced computational cost.

Unless otherwise noted, the results described in this work are for an array with row spacing $\Gamma = 200\ \mu$m, column spacing $\Lambda = 200\ \mu$m, obstacle radius $R = 50\ \mu$m, an array length of $N = 100$ unit structures, and $U_{inlet} = 100\ \mu$ms; this geometry and flow rate corresponds to those used in previously reported experiments (Gleghorn et al. 2010; Kirby et al. 2012; Smith et al. 2014; Zhu et al. 2013). Results are presented in dimensional units to facilitate ready comparison to biological length scales.

4.1 Comparison between transfer function and CFD simulations

We have validated the transfer function simulations by comparing them to the results of our previously-described CFD particle advection and cell capture simulations (Gleghorn et al. 2013; Smith et al. 2014). Devices $N = 100$ unit structures long and with various offsets Δ were studied using both CFD and transfer function simulations for cell diameters from 6 to 34 μm.

The results show that the transfer function accurately captures the collision (Fig. 3a) and capture dynamics (Fig. 3b) predicted by the CFD simulation. When considering all offsets (i.e, $\Delta = 0$ to $\Gamma/2$) and cell diameters studied, the RMS of the error residual (e.g., $P_{capture, CFD} - P_{capture, Trans. Fn.}$) was 1.01×10^{-2} row^{-1} for collision frequency and 1.34×10^{-2} for capture probability. In general, the error residual was highest for combinations of geometries and cell diameters that resulted in frequent "grazing" collision events, where a particle would be in contact with the obstacle surface for a short period of time. These small errors incurred by the transfer function simulation

(a)

(b)

(c)
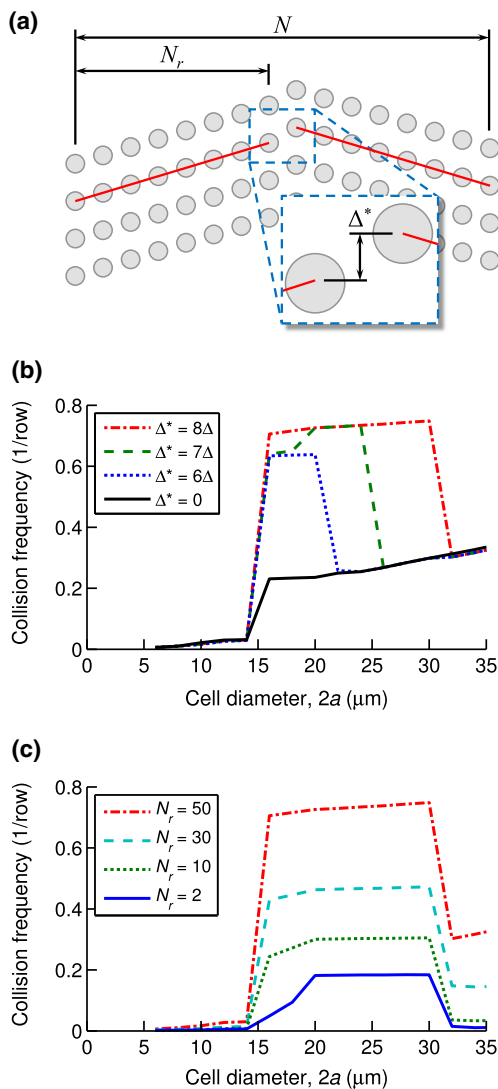
Fig. 4 The transfer function model allows for the computationally efficient simulation of reversals in the offset direction, which lead to a *notch filter* effect, reducing the collision frequency for small and large cells. **(a)** The number of rows in the device, N, the number of rows between reversals, N_r, and the y-direction shift at reversal, $\Delta^\star$, control the notch filter's performance. **(b)** The notch filter's lower diameter cutoff is proportional to Δ; the upper diameter cutoff is proportional to $\Delta^\star$ (illustrated here for $N = 100$ and $N_r = 50$). **(c)** The maximum collision frequency within the notch filter is proportional to the number of rows between reversals, N_r (shown here for $N = 100$, $\Delta^\star = 8\Delta$). Both (B) and (C) here are for a $\Delta = 8$ array

were balanced by a 74-fold computational savings as compared to the full CFD simulation.

4.2 Reversing geometries

The transfer function simulation can approximate cell transport and capture in spatially-varying obstacle arrays. One such geometry is a *reversing array* (Fig. 4a), in which the sign of the offset reverses every N_r unit structures out of N total unit structures in the device, possibly accompanied

by a y-direction shift in the obstacles following the offset reversal, $\Delta^\star$. Reversing arrays are useful in rare cell capture microdevices, as they prevent a net displacement of the target cells in the offset direction, allowing for the full area of the array to be used for cell capture; they also prevent a pressure gradient in the y direction, ensuring a better match between simulated and real-world velocity fields. Furthermore, the magnitude of $\Delta^\star$ can be selected to generate a *notch filter* in which the collision frequency of particles within a specified diameter range is much higher than for other particles; notch filters are particularly useful for systems where the contaminating cells are both smaller and larger than the target cell population.

In these simulations, the transfer function lookup tables used in Eqs. 2 to 4 are reversed in y based on the offset direction, and $\Delta^\star$ replaces Δ in Eq. 5 for the unit structure immediately following the offset reversal, as described in Section 2.2.

N, N_r, Δ, and $\Delta^\star$ all contribute to the notch filter's "width" (i.e., the lower and upper diameter cutoffs) and the

(a)

(b)
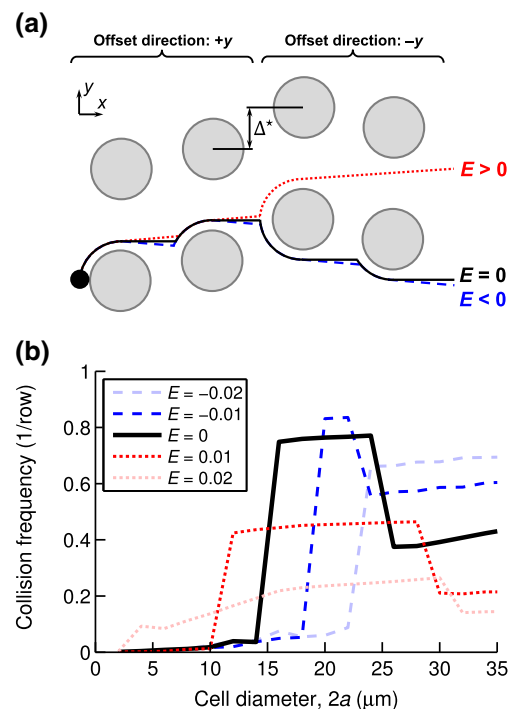
Fig. 5 (a) Off-design boundary conditions, such as from a clogged inlet channel or a lump of captured cells near the inlet, can lead to a transverse velocity error, $E = U_{\text{transverse}}/U_{\text{inlet}}$; this additional velocity component alters trajectories within the array. Here, schematic pathlines are shown in a reversing (notch filter) geometry. **(b)** As compared to $E = 0$, $E > 0$ expands the lower and upper diameter cutoffs and reduces the mean collision frequency as cells are displaced so as to miss one or more downstream obstacles; $E < 0$ increases the lower diameter cutoff and leads to an increased collision frequency for cells above the upper diameter cutoff. These effects are illustrated for $N = 100$, $N_r = 50$, $\Delta = 7 \, \mu m$, $\Delta^\star = 6\Delta$ for varying values of E

(a)

(b)

(c)
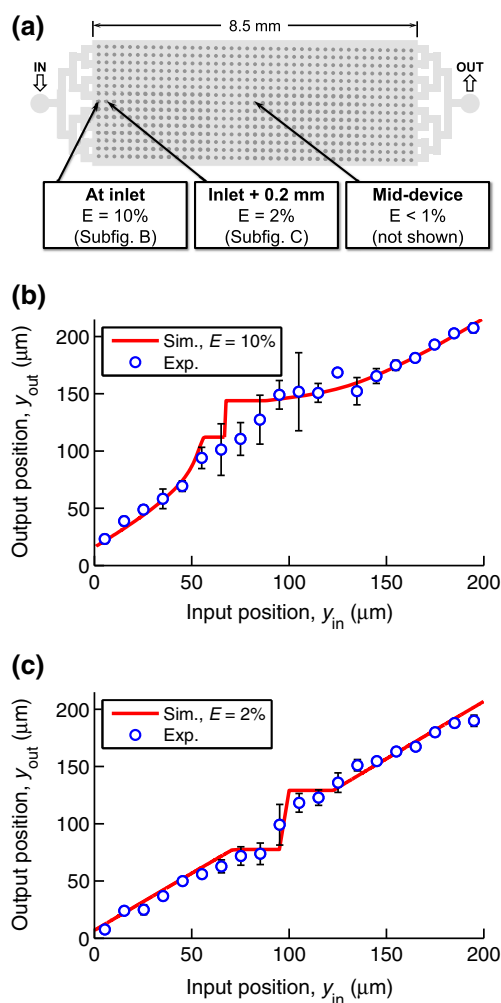
Fig. 6 **(a)** Particle tracking experiments and comparison to simulated transfer functions for various transverse errors allow for the quantification of E along the length of the obstacle array, shown in a planview schematic here (not to scale). 20 μm diameter beads were tracked through a $\Gamma = \Lambda = 200$ μm, $\Delta = 7$ μm array; the trajectories were grouped into 20 y_{in} bins and averaged within each bin, with error bars representing the standard error of the mean to a 95 % confidence interval. This data was fitted to simulated transfer functions by selecting a value of E that minimized the residual error between it and the experimental data. **(b)** Adjacent to the inlet manifold in a GEDI device, the expansion of the fluid flow to fill the obstacle array causes a large transverse error of $E = 10$ %. **(c)** The overall obstacle array is robust to these perturbations; 0.2 mm (i.e., 10 unit structures) downstream from the inlet, the error has been reduced to 2 %. Throughout the bulk of the device, $E < 1$ %

mean collision frequency for cells between the lower and upper diameter cutoffs. As is the case with non-reversing arrays (Fig. 3a), the lower diameter cutoff is a function of the offset, Δ. Figure 4b shows the effect of the y-direction shift at reversal, $\Delta^{\star}$; larger values of $\Delta^{\star}$ result in an increased upper diameter cutoff, increasing the "width" of the notch. When $\Delta^{\star}$ is sufficiently large, the obstacle following a reversal is shifted enough so that a cell that collides with the obstacle preceding it moves from one

collision to another. Small or zero values of $\Delta^{\star}$ result in a cell missing the obstacle after a reversal and traveling past several obstacles before another collision can occur, reducing the mean collision frequency. Finally, for any given Δ and N, the collision frequency within the notch filter is increased by having more unit structures between reversals, i.e., with larger values of N_r (Fig. 4c). This increase is the result of entrance effects in the array, which occur as some cells travel past several obstacles before colliding with one; more frequent reversals exacerbate this effect.

We have previously described a ballistic particle advection simulation (Gleghorn et al. 2013) that can account for reversing arrays. That ballistic approximation, which assumes that the fluid velocity field is uniform and unidirectional in x, only considers cell motion transverse to the flow direction (i.e., in the y direction) resulting from cell–obstacle collisions. The transfer function simulation, however, accounts for the transverse cell motion away from the obstacles that results from streamline dilation and contraction around the obstacles. An important conclusion of this work is that consideration of transverse cell motion owing to these dilations and contractions shows that the ballistic model underpredicts the value of $\Delta^{\star}$ needed to generate a notch filter of a given upper diameter cutoff. For example, the transfer function's more accurate estimate of collision dynamics in a reversing array with $\Delta^{\star} = 8\Delta$ yields the same upper diameter cutoff as $\Delta^{\star} = 2\Delta$ in the ballistic approximation.

4.3 Off-design boundary conditions

Understanding how cell transport in these obstacle arrays is affected by off-design boundary conditions is of practical importance when translating simulations into a robust microdevice design. These off-design boundary conditions can result from many sources; e.g., a clogged inlet channel that alters the flow within the array, or a lump of captured cells near the device inlet. They can be represented by including a transverse velocity component around the obstacles, $U_{transverse}$, and the magnitude and sign of the deviation from the on-design case represented as

$$E = \frac{U_{transverse}}{U_{inlet}}, \tag{8}$$

where positive values of $U_{transverse}$ correspond to a transverse flow component in the $+y$ direction (i.e., in the same direction as the offset for non-reversing arrays).

One approach to studying transport with these off-design boundaries is to use CFD to solve for the velocity field with various values of $U_{transverse}$, then to advect a distribution of cells through a large array as we have described previously (Gleghorn et al. 2013; Smith et al. 2014). This approach,

however, introduces another variable into the simulations, increasing the computational cost by an order of magnitude. The transfer function simulation presents a more efficient solution to this problem.

We generated transfer functions for a range of particle sizes within a $\Delta = 7$ μm array, as described in Section 2.2, with the CFD solution for one unit structure including an additional $U_{transverse}$ boundary condition. These transfer functions were then applied to study $U_{transverse}$ in a reversing array geometry.

Figure 5 shows the effect of E on the notch filter's predicted performance. Several trends are notable: First, $E < 0$ leads to an increase in the lower diameter cutoff as compared with $E = 0$. Cells which would have been deflected around the offset side of an obstacle (i.e., the $+y$ side of the obstacle for when the offset is in the $+y$ direction) by a collision event are instead deflected around the non-offset side (i.e., the $-y$ side of the obstacle for when the offset is in the $+y$ direction) due to the negative $U_{transverse}$ flow. After that deflection, the cells must travel past one or more obstacles before the array offset presents another obstacle in their path. The net effect is to reduce the mean collision frequency for cells of that size; smaller cells require less displacement to be deflected around the non-offset side of the obstacle than a larger cell, resulting in the lower diameter cutoff increasing when $E < 0$.

Second, $E < 0$ increases the mean collision frequency for cells larger than the upper diameter cutoff. As those large cells pass through a reversal in the offset direction (where there is a y-direction shift in the array, $\Delta^{\star}$), their size causes them to miss the first obstacle after the offset reversal; they then travel some distance before their next collision. $E < 0$ reduces that distance, increasing the mean collision frequency for cells larger than the upper diameter cutoff as compared to $E = 0$.

Third, $E > 0$ both broadens the notch filter (expanding the difference between the lower and upper diameter cutoffs), and reduces the mean collision frequency within the notch filter. The broadening of the notch filter is caused by cells which would have passed near the non-offset side of the obstacle being displaced by the $U_{transverse}$ flow error enough to cause a collision. Similarly, the reduction of the mean collision frequency within the notch filter is a result of cells that would have been on trajectories with frequent collisions being displaced by $U_{transverse}$ so as to miss one or more downstream obstacles, reducing the mean collision frequency.

These off-design collision dynamics represent interesting physical phenomena, and are most applicable to physical systems where many cells are captured on the obstacles and/or clog an inlet channel. They are less likely to be seen when capturing rare cells (which are few in number) at high purity; e.g., approximately 1 % of the $\mathcal{O}\left(10^4\right)$ obstacles in a GEDI microdevice will capture a cancer cell in a GEDI microdevice processing a 1 mL blood sample (Kirby et al. 2012). Furthermore, these off-design dynamics are mitigated in physical microdevices by their localized nature—that is, conservation of momentum prevents a uniform transverse flow component across the length of a device. These effects deserve careful consideration when designing a system where the number of cells captured will be on the same order as the number of obstacles, or when designing a device with few obstacles.

4.4 Experimental validation

We have measured the position transfer function at several locations (Fig. 6a) with the GEDI microdevice first reported by (Gleghorn et al. 2010); by comparing the measured transfer function to simulated transfer functions for a range of transverse flow errors, E, we can quantify E in the microdevice by selecting a simulated transfer function that minimizes the RMS residual error between it and the experimental data, as described in Section 3.

The GEDI device is designed using a branched inlet manifold; for the obstacles immediately adjacent to the inlet manifold (i.e., the first obstacles in the array), we expect significant transverse flow errors attributable to the fluid expanding from the finite number of inlet channels into the larger domain of the obstacle array. The experimental results validate this hypothesis, with bead trajectories expanding as they enter the obstacle array. Figure 6b shows the measured transfer function in this region, which corresponds to a large error of $E = 10$ % (RMS residual error for $y_{out} = 10.3$ μm).

The overall obstacle array, however, is robust to these localized errors due to the inlet and outlet manifolds. Only ten unit structures downstream of the inlet (Fig. 6c), the transverse error has been reduced to $E = 2$ % (RMS residual error = 7.7 μm). For several locations further downstream, E was measured as ≤ 1 %, indicating that the transfer function accurate simulates transport and collision phenomena (and thus the capture probably) within the bulk of the obstacle array.

5 Conclusion

This work facilitates the efficient design of application-specific rare cell capture microdevice geometries by demonstrating that a transfer function, calculated based on limited CFD and particle advection simulations for one unit structure, to predict collision and capture dynamics in arbitrarily large arrays accurately and at a 74-fold reduction in computational cost. We have shown that the transfer function approximates transport in spatially-varying arrays, and have demonstrated that a notch filter can be engineered using

reversing arrays, reducing the collision frequency for both small and large contaminants. The transfer function can be adapted to simulate off-design device conditions, such as the transverse flow component that can result from a clogged device inlet, making those studies feasible as compared to the high computational cost of a direct simulation. Finally, we have experimentally validated the transfer function approach, showing good agreement to the transfer function for polystyrene beads flowing through an obstacle array.

References

W.J. Allard, J. Matera, M.C. Miller, M. Repollet, M.C. Connelly, C. Rao, A.G.J. Tibbe, J.W. Uhr, Terstappen LWMM Tumor cells circulate in the peripheral blood of all major carcinomas but not in healthy subjects or patients with nonmalignant diseases. Clin Cancer Res **10**(20), 6897–904 (2004)

F.F. Becker, X.B. Wang, Y. Huang, R. Pethig, J. Vykoukal, P.R. Gascoyne, Separation of human breast cancer cells from blood by differential dielectric affinity. Proc Natl Acad Sci USA **92**(3), 860–864 (1995)

G.I. Bell, M. Dembo, P. Bongrand, Cell adhesion. competition between nonspecific repulsion and specific bonding. Biophys J **45**(6), 1051–1064 (1984)

A.A.S. Bhagat, H.W. Hou, L.D. Li, C.T. Lim, J. Han, Pinched flow coupled shear-modulated inertial microfluidics for high-throughput rare blood cell separation. Lab Chip **11**, 1870–1878 (2011)

D. Blair, E. Dufresne, MATLAB Particle Tracking Code http://site.physics.georgetown.edu/matlab/. Accessed 16 November 2014 (2007)

M. Cristofanilli, G.T. Budd, M.J. Ellis, A. Stopeck, J. Matera, M.C. Miller, J.M. Reuben, G.V. Doyle, W.J. Allard, L.W. Terstappen, D.F. Hayes, Circulating tumor cells, disease progression, and survival in metastatic breast cancer. N Engl J Med **351**(8), 781–791 (2004)

J. Crocker, E. Weeks, Particle Tracking Using IDL http://www.physics.emory.edu/faculty/weeks//idl/. Accessed 16 November 2014 (1996)

J. Davis, D. Inglis, K. Morton, D. Lawrence, L. Huang, S. Chou, J. Sturm, R. Austin, Deterministic hydrodynamics: Taking blood apart. Proc Natl Acad Sci USA **103**(40), 14,779–14,784 (2006)

P. Decuzzi, M. Ferrari, The adhesive strength of non-spherical particles mediated by specific interactions. Biomaterials **27**(30), 5307–5314 (2006)

M. Dembo, D.C. Torney, K. Saxman, D. Hammer, The reaction-limited kinetics of membrane-to-surface adhesion. Philos Trans R Soc London Biol **234**(1274), 55–83 (1988)

M.L. Dustin, L.M. Ferguson, P.Y. Chan, T.A. Springer, D.E. Golan, Visualization of CD2 interaction with LFA-3 and determination of the two-dimensional dissociation constant for adhesion receptors in a contact area. J Cell Biol **132**(3), 465–74 (1996)

C.M. Earhart, C.E. Hughes, R.S. Gaster, C.C. Ooi, R.J. Wilson, L.Y. Zhou, E.W. Humke, L. Xu, D.J. Wong, S.B. Willingham, E.J. Schwartz, I.L. Weissman, S.S. Jeffrey, J.W. Neal, R. Rohatgi, H.A. Wakelee, S.X. Wang, Isolation and mutational analysis of circulating tumor cells from lung cancer patients with magnetic sifters and biochips. Lab Chip **14**, 78–88 (2014)

J.P. Gleghorn, E.D. Pratt, D. Denning, H. Liu, N.H. Bander, S.T. Tagawa, D.M. Nanus, P.A. Giannakakou, B.J. Kirby, Capture of circulating tumor cells from whole blood of prostate cancer patients using geometrically enhanced differential immunocapture (GEDI) and a prostate-specific antibody. Lab Chip **10**, 27–29 (2010)

J.P. Gleghorn, J.P. Smith, B.J. Kirby, Transport and collision dynamics in periodic asymmetric obstacle arrays, Rational design of microfluidic rare-cell immunocapture devices. Phys Rev E **88**(032), 136 (2013)

A. Hatch, G. Hansmann, S.K. Murthy, Engineered alginate hydrogels for effective microfluidic capture and release of endothelial progenitor cells from whole blood. Langmuir **27**(7), 4257–4264 (2011)

D.F. Hayes, M. Cristofanilli, G.T. Budd, M.J. Ellis, A. Stopeck, M.C. Miller, J. Matera, W.J. Allard, G.V. Doyle, L.W. Terstappen, Circulating tumor cells at each follow-up time point during therapy of metastatic breast cancer patients predict progression-free and overall survival. Clin Cancer Res **12**(14), 4218–4224 (2006)

C.H. Hsu, D. Di Carlo, C. Chen, D. Irimia, M. Toner, Microvortex for focusing guiding and sorting of particles. Lab Chip **8**, 2128–2134 (2008)

C. Huang, J.P. Smith, T.N. Saha, A.D. Rhim, B. Kirby, Characterization of microfluidic shear-dependent epithelial cell adhesion molecule immunocapture and enrichment of pancreatic cancer cells from blood cells with dielectrophoresis. Biomicrofluidics **8**(4), 044107 (2014)

D. Inglis, J. Davis, R. Austin, J. Sturm, Critical particle size for fractionation by deterministic lateral displacement. Lab Chip **5**, 655–658 (2006)

B.J. Kirby, M. Jodari, M.S. Loftus, G. Gakhar, E.D. Pratt, C. Chanel-Vos, J.P. Gleghorn, S.M. Santana, H. Liu, J.P. Smith, V.N. Navarro, S.T. Tagawa, N.H. Bander, D.M. Nanus, P. Giannakakou, Functional characterization of circulating tumor cells with a prostate-cancer-specific microfluidic device. PLoS ONE **7**(4), e35,976 (2012)

R.T. Krivacic, A. Ladanyi, D.N. Curry, H.B. Hsieh, P. Kuhn, D.E. Bergsrud, J.F. Kepros, T. Barbera, M.Y. Ho, L.B. Chen, R.A. Lerner, R.H. Bruce, A rare-cell detector for cancer. Proc Natl Acad Sci USA **101**(29), 10,501–10,504 (2004)

S.T. Ligthart, F.C. Bidard, C. Decraene, T. Bachelot, S. Delaloge, E. Brain, M. Campone, P. Viens, J.Y. Pierga, L.W.M.M. Terstappen, Unbiased quantitative assessment of her-2 expression of circulating tumor cells in patients with metastatic and non-metastatic breast cancer. Annals of Oncology **24**(5), 1231–1238 (2013)

J.G. Lohr, V.A. Adalsteinsson, K. Cibulskis, A.D. Choudhury, M. Rosenberg, P. Cruz-Gordillo, J.M. Francis, C.Z. Zhang, A.K. Shalek, Satija R, Whole-exome sequencing of circulating tumor cells provides a window into metastatic prostate cancer. Natl Bio, (2014)

S. Maheswaran, D.A. Haber, Circulating tumor cells: a window into cancer biology and metastasis. Curr Opin Genet Dev **20**(1), 96–99 (2010)

S. Maheswaran, L.V. Sequist, S. Nagrath, L. Ulkus, B. Brannigan, C.V. Collura, E. Inserra, S. Diederichs, A.J. Iafrate, D.W. Bell, S. Digumarthy, A. Muzikansky, D. Irimia, J. Settleman, R.G. Tompkins, T.J. Lynch, M. Toner, D.A. Haber, Detection of mutations in egfr in circulating lung-cancer cells. New England Journal of Medicine **359**(4), 366–377 (2008). pMID: 18596266

H. Mohamed, J.N. Turner, M. Caggana, Biochip for separating fetal cells from maternal circulation. J Chromatogr A **1162**(2), 187–192 (2007)

V. Murlidhar, M. Zeinali, S. Grabauskiene, M. Ghannad-Rezaie, M.S. Wicha, D.M. Simeone, N. Ramnath, R.M. Reddy, S. Nagrath, A radial flow microfluidic device for ultra-high-throughput affinity-based isolation of circulating tumor cells. Small **10**(23), 4895–4904 (2014)

S. Nagrath, L.V. Sequist, S. Maheswaran, D.W. Bell, D. Irimia, L. Ulkus, M. Smith, E.L. Kwak, S. Digurmarthy, A. Muzikansky, P. Ryan, U. Balis, R.G. Tompkins, D.A. Haber, M. Toner, Isolation of rare circulating tumor cells in cancer patients by microchip technology. Nature **450**, 1235–1239 (2007)

N. Navin, J. Kendall, J. Troge, P. Andrews, L. Rodgers, J. McIndoo, K. Cook, A. Stepansky, D. Levy, D. Esposito, L. Muthuswamy, A. Krasnitz, W.R. McCombie, J. Hicks, M. Wigler, Tumour evolution inferred by single-cell sequencing. Nature **472**(7341), 90–4 (2011)

A.A. Powell, A.H. Talasaz, H. Zhang, M.A. Coram, A. Reddy, G. Deng, M.L. Telli, R.H. Advani, R.W. Carlson, J.A. Mollick, S. Sheth, A.W. Kurian, J.M. Ford, F.E. Stockdale, S.R. Quake, R.F. Pease, M.N. Mindrinos, G. Bhanot, S.H. Dairkee, R.W. Davis, S.S. Jeffrey, Single cell profiling of circulating tumor cells, Transcriptional heterogeneity and diversity from breast cancer cell lines. PLoS ONE **7**(5), e33,788 (2012)

E.D. Pratt, C. Huang, B.G. Hawkins, J.P. Gleghorn, B.J. Kirby, Rare cell capture in microfluidic devices. Chem Eng Sci **66**(7), 1508–1522 (2011)

E.D. Pratt, A. Stepansky, J. Hicks, B.J. Kirby, Single-cell copy number analysis of prostate cancer cells captured with geometrically enhanced differential immunocapture microdevices. Anal Chem **86**(22):11 **017**, 013–11 (2014)

E. Racila, D. Euhus, A.J. Weiss, C. Rao, J. McConnell, L.W. Terstappen, J.W. Uhr, Detection and characterization of carcinoma cells in the blood. Proc Natl Acad Sci USA **95**(8), 4589–4594 (1998)

A.D. Rhim, F.I. Thege, S.M. Santana, T.B. Lannin, T.N. Saha, S. Tsai, L.R. Maggs, M.L. Kochman, G.G. Ginsberg, J.G. Lieb, V. Chandrasekhara, J.A. Drebin, N. Ahmad, Y. Yang, B.J. Kirby, B.Z. Stanger, Detection of circulating pancreas epithelial cells in patients with pancreatic cystic lesions. Gastroenterology **146**(3), 647–651 (2014)

H.G. Russnes, H.K.M. Vollan, O.C. Lingjaerde, A. Krasnitz, P. Lundin, B. Naume, T. Sørlie, E. Borgen, I.H. Rye, A. Langerød, S.F. Chin, A.E. Teschendorff, P.J. Stephens, S. Månér, E. Schlichting, L.O. Baumbusch, R. Kåresen, M.P. Stratton, M. Wigler, C. Caldas, A. Zetterberg, J. Hicks, A.L. Børresen-Dale, Genomic architecture characterizes tumor progression paths and fate in breast cancer patients. Sci Trans Med **2**(38), 38ra47 (2010)

S.M. Santana, H. Liu, N.H. Bander, J.P. Gleghorn, B.J. Kirby, Immunocapture of prostate cancer cells by use of anti-PSMA antibodies in microdevices. Biomed Microdev **14**, 401–407 (2012)

S. Shim, K. Stemke-Hale, A.M. Tsimberidou, J. Noshari, T.E. Anderson, P.R.C. Gascoyne, Antibody-independent isolation of circulating tumor cells by continuous-flow dielectrophoresis. Biomicrofluidics **7**(1), 011807 (2013)

J.P. Smith, A.C. Barbati, S.M. Santana, J.P. Gleghorn, B.J. Kirby, Microfluidic transport in microdevices for rare cell capture. Electrophoresis **33**(21), 3133–3142 (2012)

J.P. Smith, T.B. Lannin, Y.A. Syed, S.M. Santana, B.J. Kirby, Parametric control of collision rates and capture rates in geometrically enhanced differential immunocapture (GEDI) microfluidic devices for rare cell capture. Biomed Microdev **16**(1), 143–151 (2014)

E. Sollier, D.E. Go, J. Che, D.R. Gossett, S. O'Byrne, W.M. Weaver, N. Kummer, M. Rettig, J. Goldman, N. Nickols, S. McCloskey, R.P. Kulkarni, D. Di Carlo, Size-selective collection of circulating tumor cells using vortex technology. Lab Chip **14**, 63–77 (2014)

S.L. Stott, R.J. Lee, S. Nagrath, M. Yu, D.T. Miyamoto, L. Ulkus, E.J. Inserra, M. Ulman, S. Springer, Z. Nakamura, A.L. Moore, D.I. Tsukrov, M.E. Kempner, D.M. Dahl, C.L. Wu, A.J. Iafrate, M.R. Smith, R.G. Tompkins, L.V. Sequist, M. Toner, D.A. Haber, S. Maheswara, Isolation and characterization of circulating tumor cells from patients with localized and metastatic prostate cancer. Sci Trans Med (2010)

A.H. Talasaz, A.A. Powell, D.E. Huber, J.G. Berbee, K.H. Roh, W. Yu, W. Xiao, M.M. Davis, R.F. Pease, M.N. Mindrinos, S.S. Jeffrey, R.W. Davis, Isolating highly enriched populations of circulating epithelial cells and other rare cells from blood using a magnetic sweeper device. Proc Natl Acad Sci USA **106**(10), 3970–3975 (2009)

F.I. Thege, T.N. Saha, S. Tsai, M.L. Kochman, M.A. Hollingsworth, A.D. Rhim, B.J. Kirby, Microfluidic immunocapture of circulating pancreatic cells using parallel EpCAM and MUC1 capture: characterization, optimization and downstream analysis. Lab Chip **14**, 1775–1784 (2014)

Y. Wan, J. Tan, W. Asghar, Yt. Kim, Y. Liu, S.M. Iqbal, Velocity effect on aptamer-based circulating tumor cell isolation in microfluidic devices. J Phys Chem B **115**(47), 13,891–13,896 (2011)

M. Yu, A. Bardia, N. Aceto, F. Bersani, M.W. Madden, M.C. Donaldson, R. Desai, H. Zhu, V. Comaills, Z. Zheng, B.S. Wittner, P. Stojanov, E. Brachtel, D. Sgroi, R. Kapur, T. Shioda, D.T. Ting, S. Ramaswamy, G. Getz, A.J. Iafrate, C. Benes, M. Toner, S. Maheswaran, D.A. Haber, Ex *vivo* culture of circulating breast tumor cells for individualized testing of drug susceptibility. Science **345**(6193), 216–220 (2014)

B. Zhu, J.P. Smith, M.L. Yarmush, Y. Nahmias, B.J. Kirby, S.K. Murthy, Microfluidic enrichment of mouse epidermal stem cells and validation of stem cell proliferation in vitro (Tissue Eng C, 2013)

B. Zhu, Y. Nahmias, M.L. Yarmush, S.K. Murthy, Microfluidic isolation of CD34-positive skin cells enables regeneration of hair and sebaceous glands in vivo (Stem Cells Trans Med, 2014)

C. Zhu, G. Bao, N. Wang, Cell mechancis: Mechanical response, cell adhesion, and molecular deformation. Ann Rev Biomed Eng **2**(1), 189 (2000)